# Transverse magneto-thermoelectric properties of $Fe_2CoSi$ alloy and $Fe_2CoSi$-Pt composite films

Subrata Biswas[1,2,a)], Rajkumar Modak[1,3,a)] , Takamasa Hirai[1], Ananthakrishnan Srinivasan[2], Perumal Alagarsamy[2], and Ken-ichi Uchida[1,3]

[1]*National Institute for Materials Science, Tsukuba 305-0047, Japan*
[2]*Department of Physics, Indian Institute of Technology Guwahati, Guwahati 781-039, India*
[3]*Department of Advanced Materials Science, Graduate School of Frontier Sciences, The University of Tokyo, Kashiwa 277-8561, Japan*

[a)]subra176121021@iitg.ac.in (SB), rajkumarmodak24@gmail.com (RM)

## ABSTRACT

We report a systematic evaluation of the effects of post-deposition annealing temperature and structural ordering on the anomalous Nernst effect (ANE) in $Fe_2CoSi$ (FCS) Heusler alloy thin films. The study reveals that amorphous/disordered FCS films exhibit a larger anomalous Nernst coefficient ($S_{ANE}$) compared to their crystalline counterparts, in stark contrast to conventional Co-based Heusler alloys, which typically show maximum $S_{ANE}$ in highly ordered structures. Furthermore, as a strategy for enhancing transverse thermoelectric properties, we explore $(FCS)_{100-x}Pt_x$ composite alloy films by systematically varying the Pt concentration and optimizing the composition. This method effectively enhances the transverse thermoelectric performance of the FCS-based alloys. Our findings offer valuable insights for the design and development of next-generation high-performance ANE materials.

## I. INTRODUCTION

Spin caloritronics is a multidisciplinary field that integrates principles from both spintronics and thermoelectrics.[1–3] This expanding area of investigation holds great promise for advancing our understanding of fundamental phenomena at the intersection of spin-mediated electronic and thermal transport effects.[4–7] One fascinating phenomenon of this realm is the anomalous Nernst effect (ANE), a transverse magneto-thermoelectric process wherein a charge current is generated in directions perpendicular to temperature gradient ($\nabla T$) and magnetization (**M**) of magnetic conductors.[4,8–11] ANE differs from the Seebeck effect, which generates the charge current in a direction parallel to the temperature gradient. The orthogonal relationship in ANE enables an increase in the thermoelectric output simply by enlarging the size of magnetic materials, which can be exploited to design large-area, highly flexible, and versatile energy harvesting and sensing devices.[2,7,12–15] Despite these advantages, the lower thermopower of ANE (i.e., the anomalous Nernst coefficient $S_{ANE}$) than that of the Seebeck effect (i.e., the Seebeck coefficient $S_{SE}$) is a serious impediment.[1,2,16,17]

To improve the performance of the transverse thermoelectric conversion based on ANE, researchers have investigated transport properties in various magnetic materials.[5,18–22] Ferromagnetic Heusler alloys with their unique electronic structure are promising candidates for applications of ANE.[6,20,23–26] In fact, Co-based Heusler alloys, such as $Co_2MnGa$, $Co_2MnAl_{1-x}Si_x$, have garnered considerable attention due to their large $S_{ANE}$, attributed to substantial Berry curvature near the Fermi level.[6,19,27] However, to achieve a highly ordered crystal structure necessary for realizing large ANE in these Co-based Heusler alloys, the as-prepared alloys have to be annealed at high temperatures. In this regards, Reichlova *et al.* reported a large ANE in $Co_2MnGa$ thin films grown and annealed at 500°C.[19] Similarly, Breidenbach *et al.* investigated the ANE in epitaxial $Co_2MnAl_xSi_{1-x}$ and $Co_2FeAl$ Heusler alloy thin films grown on MgO seed layers, followed by annealing at 600°C to improve crystallinity.[25] Furthermore, Sakuraba *et al.* systematically studied the effect of atomic ordering on the giant ANE in $Co_2MnAl_{1-x}Si_x$ Heusler alloys by annealing the films between 500°C and 700°C.[6] This process poses significant obstacle in the mass production of these Heusler alloys for practical thermoelectric applications. Noky *et al.* carried out an extensive theoretical study on the intrinsic anomalous transport properties of Heusler compounds, predicting that some Fe-based Heusler alloys could exhibit significant ANE and anomalous Hall effect (AHE).[28,29] Supporting these predictions, experimental results have shown that compounds such as $Fe_2CoAl$, $Fe_2CoGa$, $Fe_2NiAl$, and $Fe_2NiGa$ possess anomalous Hall conductivity values

ranging from 250 to 750 S/cm. Despite these encouraging results, research on ANE in Fe-based Heusler alloys remains limited, and their full potential for transverse magneto-thermoelectric conversion is yet to be fully explored.

In addition to exploring new magnetic materials exhibiting large $S_{ANE}$, efforts to enhance the performance of ANE have been made by fabricating an artificial magnetic structure within existing material combinations.[1,2,7,10,22,30–33] Alternating layers of ferromagnetic (FM) and nonmagnetic (NM) thin films are an effective strategy to enhance $S_{ANE}$. In this regard, Uchida *et al.* have demonstrated that FM/NM multilayers consisting of Fe/Pt, Fe/Au, and Fe/Cu exhibit larger $S_{ANE}$ than the single-layer Fe film and that the $S_{ANE}$ value increases when the interface density of the multilayers is increased.[31] They have also reported that the enhancement observed for Fe/Pt is higher than that of Fe/Au and Fe/Cu in the multilayers with the same interface density, which may be attributed to the strong spin-orbit coupling of the heavy metal (HM) Pt. Similar enhancements in $S_{ANE}$ with the interface density have been reported in Co/Pt multilayers[33] and Ni/Pt superlattices.[10] Interface-induced ANE enhancement has also been observed in $Fe_3O_4$/Pt multilayers, where sub nanometer Fe-Pt interdiffusion is believed to play a significant role.[32] While previous studies focused on increasing the FM/NM interfaces to improve ANE performance, the evaluation of FM-NM composites that incorporate a heavy metal as the NM to enhance spin orbit interaction remains limited. These composites, which possess the maximum number of interfaces and potentially greater interdiffusion, remain largely unexplored.

In this study, we present a detailed investigation on the transverse magneto-thermoelectric properties of $Fe_2CoSi$ (FCS) Heusler alloy films aimed at evaluating the effects of post-deposition annealing temperature and the subsequent improvement in structural ordering on their transverse thermoelectric performance. To explore strategies for enhancing this performance, we further examined $(FCS)_{100-x}Pt_x$ composite alloy films by systematically varying the Pt concentration and optimizing the composition. For efficient optimization, we employed a high-throughput material screening approach based on combinatorial materials science and thermal imaging of the anomalous Ettingshausen effect (AEE), which is the reciprocal of ANE, using lock-in thermography (LIT).[4,8,13,14,30,34–38] Finally, uniform $(FCS)_{100-x}Pt_x$ composite alloy films with the optimized composition were fabricated to evaluate their transverse thermoelectric performance. This systematic study not only assesses the ANE behavior of FCS Heusler alloys but also provides a valuable guideline for the future development of high-performance ANE materials.

## II. EXPERIMENTAL DETAILS

### A. Fabrication of uniform FCS and $(FCS)_{100-x}Pt_x$ composition gradient film

Uniform FCS films with a thickness of 50 nm were deposited on a single-crystalline MgO (001) substrate at room temperature using a magnetron sputtering system. Prior to deposition, the sputtering chamber was evacuated to a base pressure below $2\times10^{-6}$ Pa, and the substrate surfaces were treated *in situ* with low-power Ar-ion milling for 20 minutes to improve the substrate interface. FCS thin films were then deposited at room temperature by co-sputtering Fe, Co, and Si targets, using radio frequency (RF) power sources for Fe and Co and a direct current (DC) power source for Si, at an Ar gas pressure of 0.6 Pa. Following deposition, *in situ* post-deposition annealing was performed for 30 minutes under vacuum at three temperatures, viz., $T_a$ = 250 °C, 350 °C, and 450 °C. To prevent oxidation, the as-deposited films were capped with a 2 nm-thick Al layer before annealing. The elemental composition of all FCS films was confirmed to be Fe:Co:Si ≈ 2:1:1 by X-ray fluorescence spectrometry. The as-deposited and annealed FCS films of identical compositions were used for evaluation.

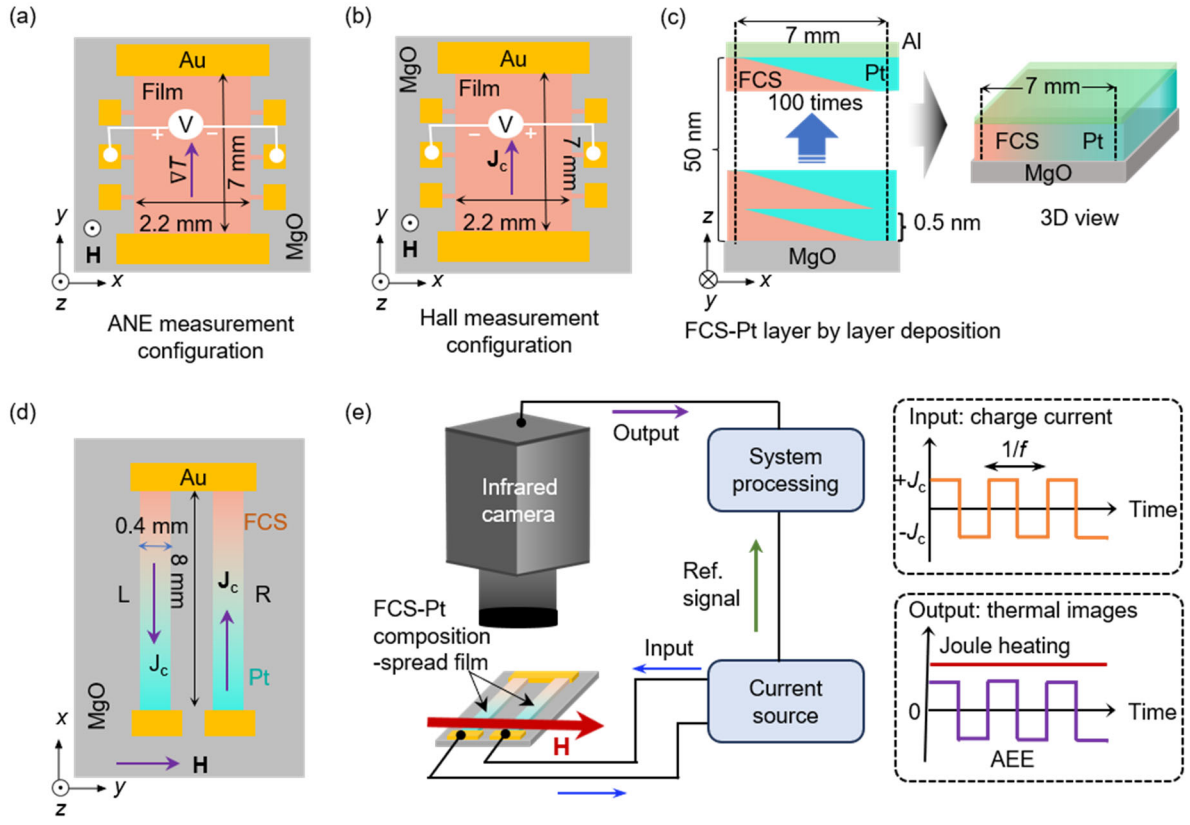


Fig. 1. (a) Schematic of the measurement configuration used for the anomalous Nernst effect (ANE). ∇*T* is the temperature gradient and **H** is the magnetic field vector with the magnitude of *H*. (b) The schematic of the Hall measurement configuration used to probe the anomalous

Hall effect (AHE) under an out-of-plane magnetic field. Here, $\mathbf{J}_c$ is the charge current vector applied along the length of the film. (c) Deposition protocol of $(FCS)_{100-x}Pt_x$ composition-spread film with wedge-shaped layer-by-layer deposition of FCS and Pt using a linearly moving shutter. (d) Lithographically patterned configuration for the measurement of the composition dependence of the anomalous Ettinghausen effect (AEE) in $(FCS)_{100-x}Pt_x$ films. (e) Schematic of the AEE measurement system with different electrical components.

The $(FCS)_{100-x}Pt_x$ composition-gradient films with a thickness of 50 nm were fabricated on a single-crystalline MgO (001) substrate. To achieve a composition variation of $0 \leq x \leq 100$ at.% over a length of 7.0 mm on a single substrate, the films were prepared from Fe, Co, Si, and Pt targets using a layer-by-layer wedge-shaped deposition process established in earlier studies.[20,30,39] The process involves three steps, viz., (i) deposition of a wedge-shaped FCS film with a thickness gradient of 0.0–0.5 nm over a length of 7.0 mm using a linearly moving shutter, (ii) rotation of the substrate by 180º, and (iii) deposition of a wedge-shaped Pt layer with the thickness gradient of 0.0–0.5 nm over a length of 7.0 mm. The sequence (i) – (iii) forms a flat $(FCS)_{100-x}Pt_x$ composition gradient film of thickness 0.5 nm. This sequence was repeated 100 times to get the 50 nm-thick $(FCS)_{100-x}Pt_x$ composition-gradient film [see Fig. 1(c)]. The deposition condition for the FCS film in step (i) was kept identical to the condition used for uniform FCS films discussed in experimental section A. A DC power source was used to deposit Pt. The deposition was carried out at room temperature, and the as-deposited films were capped with a 2 nm-thick Al layer.

## B. Measurements of structural and transport properties for uniform films

The structural ordering in as-deposited and annealed FCS films was evaluated using X-ray diffraction (XRD) with a Cu $K_\alpha$ X-ray source (Rigaku Smartlab, $\lambda = 0.15406$ nm) in Bragg-Brentano geometry. For the measurements of AHE and ANE, the films were patterned into a Hall bar structure with a width of 2.2 mm by photolithography, as depicted in Fig. 1(a, b). For the measurement of ANE, an out-of-plane magnetic field $\mathbf{H}$ and an in-plane $\nabla T$ were applied to the film, and the $\mathbf{H}$ dependence of the transverse voltage $V$ was recorded along the direction perpendicular to both $\mathbf{H}$ and $\nabla T$ at different $\nabla T$ values. The value of $\nabla T$ was estimated by recording a steady-state temperature profile of the films using an infrared camera, a technique established in earlier studies.[6,12,40,41] To ensure uniform emissivity, the surface of the FCS films was coated with black ink before the temperature profile measurement.

Figure 1(b) schematically shows the configuration employed for Hall-effect

measurements. The Hall resistivity $\rho_H$ was measured by applying a charge current of 100 μA in the length direction of the Hall bar and sweeping **H** perpendicular to the film plane. The electrical resistivity $\rho_{xx}$ and Seebeck coefficient $S_{SE}$ of the films were measured using the electrical resistance/Seebeck coefficient measurement system (ADVANCE RIKO, ZEM-3). All the measurements were performed at room temperature (~300 K).

### C. LIT measurement

For performing the AEE measurement using the LIT technique, the $(FCS)_{100-x}Pt_x$ composition-gradient film was patterned into a device consisting of two $(FCS)_{100-x}Pt_x$ composition-gradient rectangular wires with a width of 0.4 mm and a length of 8.0 mm, where the composition gradient was along the length ($x$-direction) [see Fig. 1(d)]. During the LIT measurement, the wires were electrically connected in series, with a charge current flowing in opposite directions along the length. The magnetic field was applied along the width direction of the wires ($y$-direction). In this condition, the temperature modulation is generated on the sample surface due to the AEE-induced heat current along the thickness direction. The infrared radiation thermally emitted from the sample surface was detected while applying a square-wave-modulated AC charge current with a square-wave amplitude of 25 mA, frequency $f$ = 10 Hz, and zero DC offset along the wires and an external magnetic field $\mu_0 H$ of ± 0.5 T, where $\mu_0$ is the vacuum permeability. To extract the pure AEE contribution from other thermoelectric background signals, we employed the previously established procedures.[20,30,36,37] Accordingly, lock-in amplitude $A$ and phase $\phi$ images showing the distribution of the current-induced temperature modulation with the $H$-odd dependence were obtained by subtracting the raw LIT images for **M** || +$y$ from those for **M** || -$y$ and dividing the subtracted images by 2. The temperature modulation due to Joule heating was recorded by applying a square-wave-modulated AC charge current with the square-wave amplitude of 12.5 mA, frequency $f$ = 10 Hz, and 12.5 mA DC offset in the absence of an external magnetic field. A schematic diagram of the LIT measurement system is shown in Fig. 1(e).

## III. RESULTS AND DISCUSSIONS

### A. Dependence of transverse thermoelectric properties on structural ordering in single-layer FCS films

To investigate the relationship between structural stability, atomic disorder, and thermoelectric

properties in FCS films, we fabricated 50-nm-thick FCS films at different post-deposition annealing temperatures, $T_a$. XRD patterns of the as-deposited and annealed FCS films are shown in Fig. 2(a, b). The as-deposited film exhibits no discernible XRD peaks, indicating its amorphous nature. The presence of superlattice 002 and 004 peaks in the XRD pattern [see Fig. 2(a)] confirms evolution of crystalline ordering in annealed FCS films with a (001) preferred growth direction.

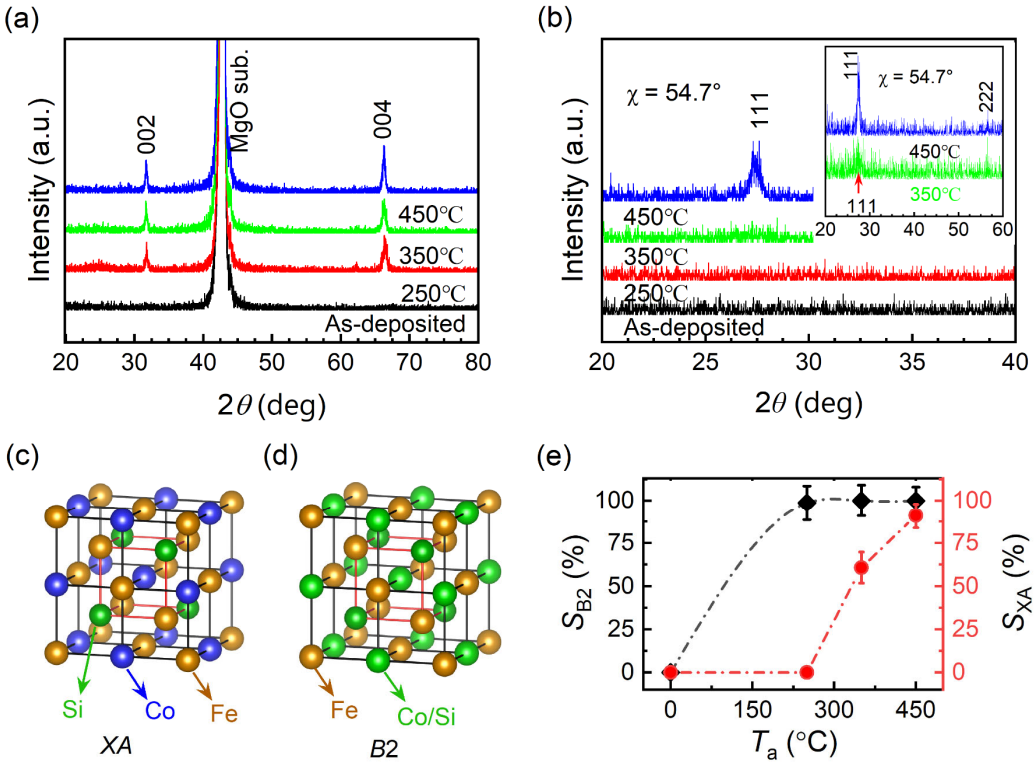


Fig. 2. (a) XRD patterns (ω-2$\theta$ scan, out-of-plane) of the as-deposited and annealed $Fe_2CoSi$ (FCS) films. (b) ω-2$\theta$ scan of the films oriented at $\chi \approx 54.7°$ depicting (111) superlattice reflection. Inset of (b) shows the 111 peaks for FCS thin films annealed at $T_a$ = 350 °C and 450 °C, plotted with an enlarged intensity scale. (c) Unit cell of *XA*-type FCS alloy. (d) Unit cell of disordered *B2*-type FCS alloy. (e) Estimated degree of *XA*- and *B2*-type ordering in the as-deposited FCS film and the films annealed at different $T_a$, where the as-deposited FCS film is shown at $T_a$ = 0 °C.

To quantitatively evaluate the evolution of crystalline ordering with $T_a$, we further examined the XRD pattern in the (111) direction by tilting the sample stage by 54.7° from the out-of-plane direction to record the 111 superlattice peak. As shown in Fig. 2(b), the 111 superlattice peak is absent in the XRD patterns of the as-deposited film and the film annealed at $T_a$ = 250 °C. However, a weak 111 superlattice peak is observed for the film annealed at $T_a$

= 350 °C (see inset of Fig. 2(b)), indicating the onset of chemical ordering. The 111 peak becomes clearly pronounced for $T_a$ = 450 °C, reflecting enhanced *XA* ordering with increasing $T_a$. A faint fundamental 222 peak also appears for the $T_a$ = 350 °C and $T_a$ = 450 °C films. The 002 and 111 superlattice peaks provide information about the degree of atomic ordering in Heusler alloys, which can be quantified using the following formula[42],

$$\left(\frac{I_{002}}{I_{004}}\right)_{\text{exp.}} = S_{\text{B2}}^2 \left(\frac{I_{002}}{I_{004}}\right)_{\text{cal.}} ; \qquad \left(\frac{I_{111}}{I_{004}}\right)_{\text{exp.}} = \left[S_{\text{XA}}\left(\frac{2 - S_{B2}}{2}\right)\right]^2 \left(\frac{I_{111}}{I_{004}}\right)_{\text{cal.}} \tag{1}$$

where, $I_{002}$, $I_{004}$, and $I_{111}$ represent the integrated intensities of the 002, 004, and 111 peaks, respectively, and $S_{\text{B2}}$ and $S_{\text{XA}}$ represent the degrees of *B*2 and *XA* ordering, respectively. It is worthy to note that the fully ordered FCS alloy is known to form an *XA*-type (space group $F\bar{4}3m$) inverse Heusler alloy structure.[43,44] The subscripts exp. and cal. represent the values obtained from the experimental and simulated XRD patterns for an ideal *XA* structure [Fig. 2(c)], respectively. The *B*2 order represents the exchange of crystalline sites between Si and Fe/Co atoms [Fig. 2(d)]. To calculate $S_{\text{B2}}$ and $S_{\text{XA}}$ parameters using Eq. (1), we performed powder XRD pattern simulations for a fully *XA*-ordered FCS alloy using the "visualization for electronic and structural analysis" software. To compare the simulated powder XRD pattern with the experimental out-of-plane XRD data for the epitaxial films, appropriate multiplicity factors were used for the 002, 004, and 111 peaks.

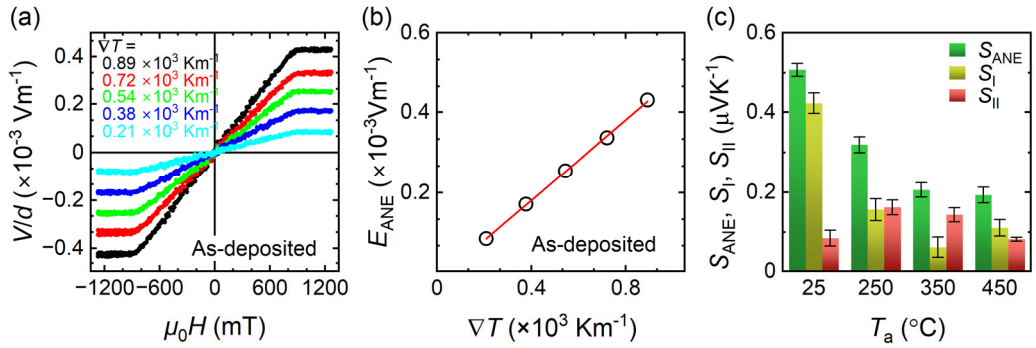


Fig. 3. (a) *H* dependence of the transverse voltage *V* divided by the distance between the voltage probe electrodes *d* (i.e., *V*/*d*) at various values of $\nabla T$ for the as-deposited FCS film. (b) $\nabla T$ dependence of the transverse electric field generated by ANE (i.e., $E_{\text{ANE}}$) of the as-deposited film. (c) Extracted ANE coefficient, $S_{\text{ANE}}$, $S_{\text{I}} = \rho_{xx}\alpha_{xy}$ and $S_{\text{II}} = \rho_{xy}\alpha_{xx}$. $\alpha_{xx}$ ($\alpha_{xy}$) is the longitudinal (transverse) component of the thermoelectric conductivity.

The obtained $S_{\text{B2}}$ and $S_{\text{XA}}$ parameters are summarized in Fig. 2(e). The $S_{\text{B2}}$ and $S_{\text{XA}}$ values for the as-deposited film were observed to be zero, indicating an amorphous structure, and

gradually increasing with increasing annealing temperature, indicating the formation of ordered structures. These results suggest that a highly ordered *XA*-type structure can be obtained from the as-deposited amorphous FCS film by annealing it at $T_a \geq 450$ °C for 30 minutes. Further, the improvement in the crystalline order is reflected in the increase in $M_s$ values from 446 emu/cc in the as-deposited film to 1030 emu/cc in the 450°C annealed film. A detailed discussion of the magnetization data is provided in the supplementary material (see Note S2).

Now, we focus on investigating the influence of structural ordering on the transverse thermoelectric properties of the FCS films. To compare these properties, we determined the anomalous Nernst coefficient ($S_{ANE}$) for the as-deposited and annealed FCS films. $S_{ANE}$ was determined by measuring the temperature gradient $\nabla T$-dependent ANE-induced electric field $E_{ANE}$ using the relationship:[6]

$$\mathbf{E}_{ANE} = S_{ANE} \nabla T \times \frac{\mathbf{M}}{|\mathbf{M}|} \quad (2)$$

where **M** is the magnetization vector with a magnitude of *M*. Figure 3(a) shows the *H* dependence of *V*/*d* with *d* being the distance between the voltage probe electrodes, recorded at different $\nabla T$ values for the as-deposited film. To determine $S_{ANE}$, the field-odd component of $E_{ANE}$ was extracted for each $\nabla T$ value from the *H* dependence of *V*/*d* for all the films. We estimated this component by finding the zero-field intercept of the linear fit to the *V*/*d* versus *H* data in the saturation (High field) region for each $\nabla T$. The $\nabla T$ dependence of $E_{ANE}$ of the as-deposited film is shown in Fig. 3(b), from which the $S_{ANE}$ was estimated from the slope of the linear fit passing through the origin. The obtained $S_{ANE}$ values for the as-deposited and annealed FCS films using this procedure are presented in Fig. 3(c). These results reveal an unconventional trend, viz., while large $S_{ANE}$ is typically observed in highly ordered crystalline Co-based Heusler alloys,[6,21,24,45] the present FCS films exhibit the largest $S_{ANE}$ value for the as-deposited amorphous film, which gradually decreases with increasing crystalline ordering.

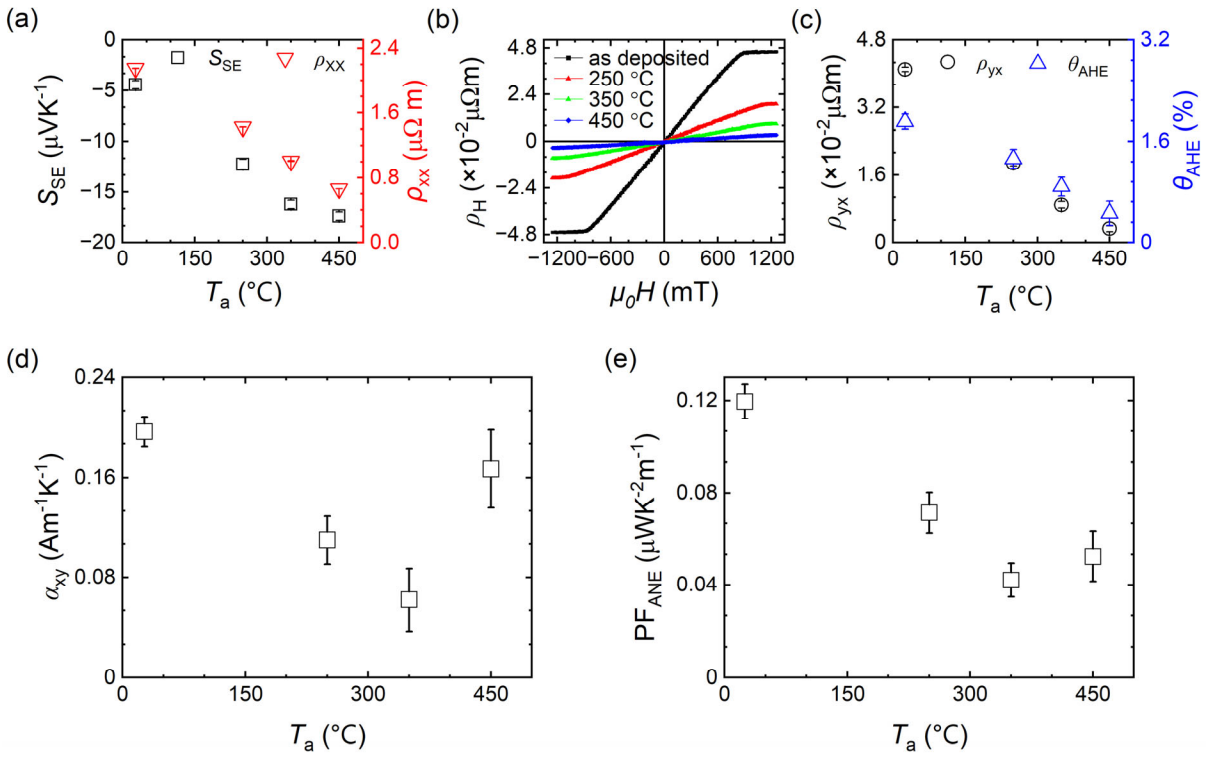


Fig. 4. (a) Seebeck coefficient $S_{SE}$ and electrical resistivity $\rho_{xx}$ of the FCS films as a function of $T_a$. (b) $H$ dependence of the Hall resistivity $\rho_H$ for the films annealed at different $T_a$. (c) Anomalous Hall resistivity $\rho_{yx}$ and anomalous Hall angle ($\theta_{AHE}$) as a function of $T_a$. (d) Transverse thermoelectric conductivity $\alpha_{xy}$ with different $T_a$. (e) Power factor of ANE (PF$_{ANE}$) as a function of $T_a$.

To understand the mechanism and investigate the factors responsible for this unusual behavior observed in FCS films, we evaluated the different contributions to $S_{ANE}$, following previous reports.[6,30] $S_{ANE}$ is usually expressed as

$$S_{ANE} = S_I + S_{II} = \rho_{xx}\alpha_{xy} - S_{SE}\rho_{yx}/\rho_{xx} \quad (3)$$

Here, $\rho_{xx}$, $\alpha_{xy}$, $S_{SE}$, and $\rho_{yx}$ are the electrical resistivity, transverse thermoelectric conductivity, Seebeck coefficient, and anomalous Hall resistivity, respectively. Although, in general, Eq. (3) includes both ordinary and anomalous components, only the magnetization dependent anomalous component is considered in this study. We measured $\rho_{xx}$, $S_{SE}$, and $\rho_{yx}$ for the films to estimate the $S_I$ and $S_{II}$ contributions. $\rho_{xx}$ and $S_{SE}$ of the films are shown in Fig. 4(a). The magnitude of $S_{SE}$ increases with increasing $T_a$, reaching −17.4 μV K$^{-1}$ for the film annealed at $T_a$ = 450 °C. The observed $S_{SE}$ value for *XA*-ordered FCS film is comparable with those of other Fe-based ordered Heusler alloys, such as Fe$_2$CoAl ($S_{SE}$ = −17.5 μVK$^{-1}$), Fe$_2$NiAl (−15 μVK$^{-1}$), and Fe$_2$NiGa (−19.3 μVK$^{-1}$).[24,46] The $\rho_{xx}$ value monotonically decreases with an

increase in $T_a$, which is attributed to the improved crystalline order of the FCS films with increasing $T_a$. The $\rho_{xx}$ value of the FCS film annealed at $T_a$ = 450 °C (0.71 μΩ m) is comparable with the value reported previously in ordered FCS films.[47] Figure 4(b) shows the out-of-plane $H$ dependence of $\rho_H$ for the as-deposited and annealed FCS films at various $T_a$ values. The $\rho_{yx}$ values were then estimated from the $H$-odd dependence of the $\rho_H$ data at saturation. Figure 4(c) displays the $\rho_{yx}$ and anomalous Hall angle, $\theta_{AHE} = \rho_{yx}/\rho_{xx}$, values for the as-deposited and annealed FCS films at various $T_a$ values. Similar to $S_{ANE}$, both $\rho_{yx}$ and $\theta_{AHE}$ are largest for the as-deposited amorphous/disordered FCS film and gradually decrease in the films with increased crystalline ordering achieved due to annealed at higher $T_a$. From these experimentally obtained values of $S_{ANE}$, $S_{SE}$, $\rho_{xx}$, $\rho_{yx}$, we estimated $S_I$ and $S_{II}$, which are summarized in Fig. 3(c). The data reveal that, for both as-deposited and annealed FCS films, $S_{ANE}$ is dominated by the $S_I$ term, due to the combined effect of $\rho_{xx}$ and $\alpha_{xy}$. The data also reveal that the large $S_{ANE}$ in the as-deposited FCS film is due to a large $S_I$ compared to that for the annealed films, which can be correlated with the larger $\rho_{xx}$ for the amorphous/disordered as-deposited FCS film compared to its ordered crystalline phase counterparts. It is worth mentioning that no systematic $T_a$ dependence is observed in the $S_I$ term of the annealed FCS films. However, a gradual decrease in the $S_{II}$ term is observed with increasing $T_a$ due to the rapid decrease in $\theta_{AHE}$ despite the gradual increase in $S_{SE}$ (except for the as-deposited FCS film, for which the very small $S_{SE}$ value results in the smallest $S_{II}$ despite the maximum $\theta_{AHE}$). To further clarify the origin of the large $S_I$ term for the as-deposited FCS film, we further evaluated $\alpha_{xy}$ using the relation $\alpha_{xy} = S_I/\rho_{xx}$, and found that it is largest for the as-deposited film. Here again, no systematic correlation is observed with $T_a$ [see Fig. 4(d)]. However, the detailed investigation of the different components in $S_{ANE}$ clearly reveals that the large $\rho_{xx}$ and $\alpha_{xy}$ are responsible for the large $S_I$ term for the as-deposited FCS film, with large $\rho_{xx}$ being the major contributor.

To evaluate the ANE performance of a material, not only is a large $S_{ANE}$ value important, but the evaluation of the power factor ($PF_{ANE}$), represented by $S_{ANE}^2/\rho_{xx}$, is also necessary. Therefore, we evaluated $PF_{ANE}$ for the FCS films and the results obtained are presented in Fig. 4(e). $PF_{ANE}$ exhibits its maximum value for the as-deposited FCS film and gradually decreases with increasing $T_a$, following the same trend observed in $S_{ANE}$. While the observed $S_{ANE}$ and $PF_{ANE}$ values are lower than those reported for many conventional and *XA*-type ordered Fe-based Heusler alloy films,[6,19,20,24] these results offer a new perspective that diverges from the conventional approach of focusing on highly ordered Heusler alloys to achieve large ANE.

This study indicates the unconventional behavior that amorphous/disordered Heusler alloys exhibit larger ANE than their ordered crystalline counterparts. The amorphous nature of such alloys is expected to offer advantages in fabrication and application flexibility.

**B. Evaluation of FCS-Pt composite alloy films**

To explore the possibility of further improving $S_{ANE}$ of the as-deposited amorphous/disordered FCS films, we evaluated FCS-Pt composite alloys. Since we observed the maximum $S_{ANE}$ for the as-deposited amorphous/disordered FCS film, we focused only on FCS-Pt composite alloy films deposited at room temperature. To determine the optimum ratio of FCS and Pt, we systematically varied Pt at.% from 0 to 100% and evaluated transverse thermoelectric properties of the $FCS_{100-x}Pt_x$ composite alloy system. The systematic variation of $x$ by preparing many films involves time-consuming experiments and puts a large demand on material and experimental resources. Further, the finite number of test films also limits the determination of the best composition accurately. Therefore, for a better and efficient optimization process, we adopted the previously established procedure of high throughput evaluation of transverse thermoelectric materials utilizing the composition gradient films and LIT technique based on active infrared imaging.[14,20,30,36-38] A composition gradient film has a continuous variation of $x$ and eliminates the requirement of fabrication of several films, thus reducing the time, material, and resource consumption. For this purpose, a composition gradient $FCS_{100-x}Pt_x$ composite alloy film was deposited on a single-crystalline MgO(100) substrate at room temperature (see the experimental section A for the detailed procedure of the film fabrication). However, the direct measurement of ANE for such a composition-spread film requires the preparation of many Hall bar-type structures to investigate the composition ($x$) dependence of ANE. Since there is a limitation on the number of Hall bars made along the composition gradient to reduce difficulty in ANE measurements, it limits the minimum composition difference between two successive bars. Moreover, one-by-one thermopower measurements take a long time. The LIT imaging detection enables high-throughput material screening for ANE through the measurement of its Onsager reciprocal, viz., AEE. The AEE measurement using LIT requires only a simple strip along the composition gradient as shown in Fig. 1(d), thus enabling easy and efficient scanning for the best composition region in a composition-spread film. Importantly, the AEE data is continuous along the composition gradient, which gives a much accurate composition dependence of ANE/AEE. Therefore, to efficiently evaluate the magneto-thermoelectric conversion property of the $FCS_{100-x}Pt_x$

composition-gradient film, AEE was measured along the composition gradient using the LIT technique (see experimental section C for LIT measurement procedure).

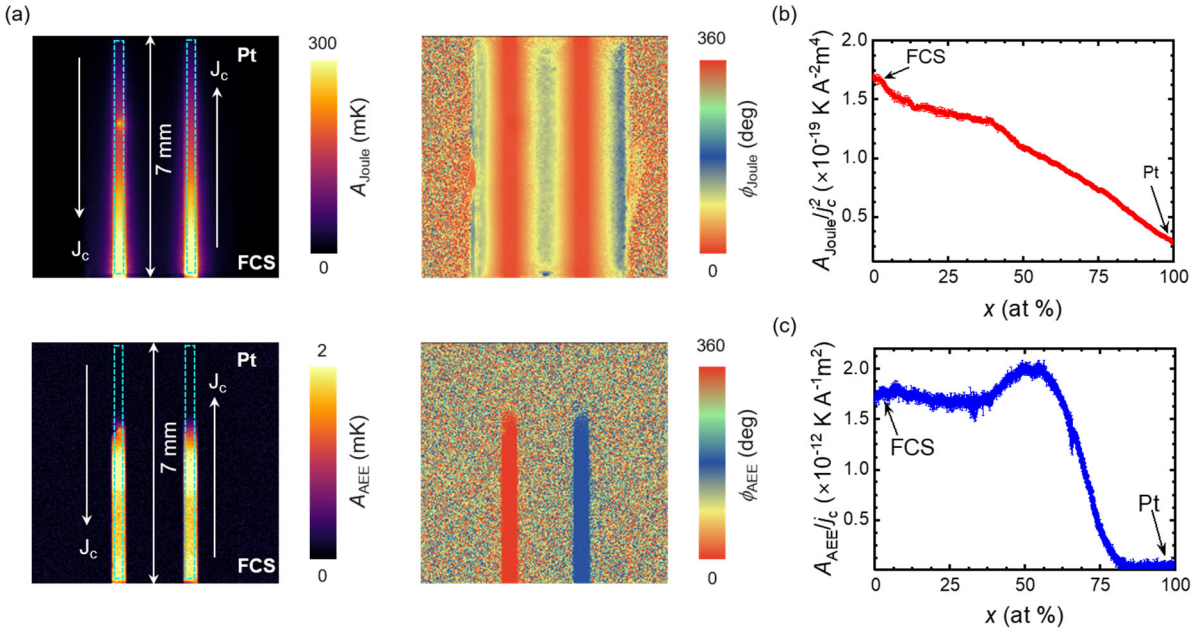


Fig. 5. (a) Temperature-modulated $A_{Joule}$ and $\phi_{Joule}$ induced by Joule-heating (upper row) at $f$ = 25 Hz, and $J_c$ = 25 mA. $A_{AEE}$ and $\phi_{AEE}$ images generated (lower row) at $f$ = 10 Hz, $J_c$ = 25 mA, and $\mu_0 H$ = 0.5 T along the film plane. Variations of (b) $A_{Joule}/j_c^2$, and (c) $A_{AEE}/j_c$ with Pt at.% in the FCS$_{100-x}$Pt$_x$ composition-gradient film.

Figure 5(a) shows the $A$ and $\phi$ images of the temperature modulation due to the Joule heating (defined as $A_{Joule}$ and $\phi_{Joule}$) and AEE (defined as $A_{AEE}$ and $\phi_{AEE}$), respectively. The $A_{Joule}$ value is proportional to the local resistivity in our configuration because the charge current density $j_c$ is uniform and the heat loss from the film to the substrate is independent of the position.[20] Figure 5(b) presents the $x$ dependence of $A_{Joule}/j_c^2$ for the FCS$_{100-x}$Pt$_x$ composition-gradient film extracted by averaging $y$-directional line profiles of the $A_{Joule}$ image on the sample area represented by the rectangle box in Fig. 5(a). Variation of $A_{Joule}/j^2_c$ with $x$ shows a nearly linear decreasing trend with an increase in $x$ (Pt at.%) content in the (FCS)$_{100-x}$Pt$_x$ composite film. This tendency is consistent with the fact that FCS has higher resistivity than Pt and the Pt volume fraction increases with increasing $x$. Figure 5(c) displays the $x$ dependence of $A_{AEE}/j_c$ for the (FCS)$_{100-x}$Pt$_x$ composition-gradient film extracted by averaging $y$-directional line profiles of the $A_{AEE}$ image obtained by extracting the $H$-odd component of the detected LIT images.[14,20,30,37] The result readily shows that around $x$ = 50 at.%, the maximum AEE-induced temperature modulation can be observed revealing the optimum

composition for best AEE performance to be $(FCS)_{50}Pt_{50}$ for the $(FCS)_{100-x}Pt_x$ composite alloy system. While this high throughput screening of $(FCS)_{100-x}Pt_x$ composite alloys qualitatively suggests the optimum composition for the FCS-Pt composite and a possible enhancement of ANE signals based on the reciprocal relationship with AEE and ANE, the direct measurement of ANE in these alloys is necessary to quantitatively evaluate the enhancement in transverse thermoelectric performance of the alloy.

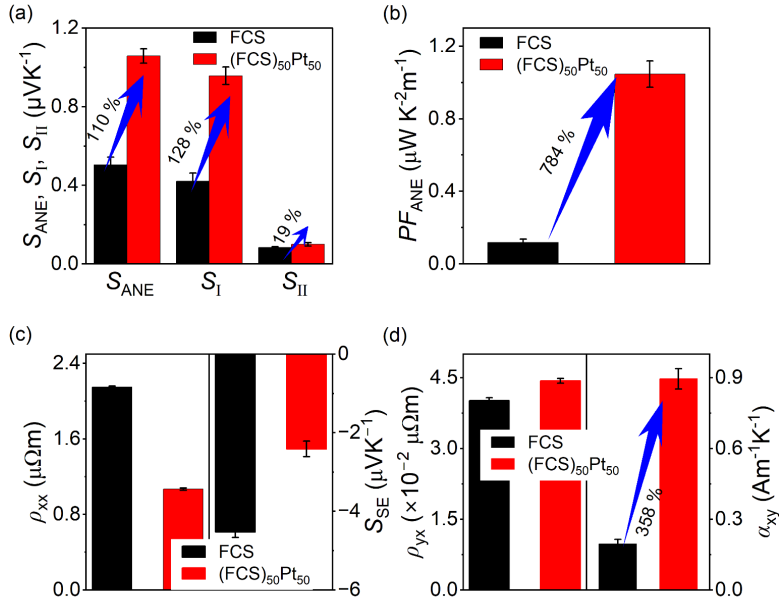


Fig. 6. (a) Extracted ANE coefficient, $S_{ANE}$, $S_I$ and $S_{II}$, (b) power factor $PF_{ANE}$, (c) $\rho_{xx}$ and $S_{SE}$, (d) $\rho_{yx}$ and $\alpha_{xy}$ of as-deposited FCS (black) and $(FCS)_{50}Pt_{50}$ (red) thin film.

To quantitatively evaluate the transverse thermoelectric performance of the optimized FCS-Pt composite system, we fabricated a uniform $(FCS)_{50}Pt_{50}$ film by ultra-thin [FCS (0.5 nm)/Pt (0.5 nm)]$_{100}$ stacks, resembling the fabrication process of composition gradient film as well as by co-sputtering. It has been previously reported that layer by layer deposition of ultra-thin layers induces atomic intermixing at the microstructural level, resulting in composite formation.[30] The measurement condition and the analysis process used to determine $S_{ANE}$ are identical to those described in the previous section. The observed $S_{ANE}$ value for the uniform $(FCS)_{50}Pt_{50}$ film is shown in Fig. 6(a) and compared with that of the as-deposited FCS film. As can be seen from Fig. 6(a), nearly two times larger $S_{ANE}$ is observed for the $(FCS)_{50}Pt_{50}$ composite alloy as compared to pure FCS. The observed $S_{ANE}$ of ~1.07 μV $K^{-1}$ for the $(FCS)_{50}Pt_{50}$ composite is comparable to those reported for various amorphous thin films[30], and Fe-based ordered Heusler alloys such as $Fe_2NiGa$, $Fe_2NiAl$, $Fe_2CoGa$.[24] The value of $S_{ANE}$ obtained for the $(FCS)_{50}Pt_{50}$ composite film is comparable to or higher than the values reported

for well-established Fe/Pt and Co/Pt composite/multilayer systems, which typically exhibit $S_{ANE}$ values in the range of 0.56 μV $K^{-1}$ to 1.2 μV $K^{-1}$, depending on thickness, interface density, and measurement geometry at room temperature.[31,33,48] There is no significant difference in $S_{ANE}$ observed between the $(FCS)_{50}Pt_{50}$ fabricated by layer by layer deposition and co-sputtering. This result is consistent with previous reports which show that atomic mixing occurs in ultrathin multilayer films and such systems behave as a single alloy composite.[30] Furthermore, $PF_{ANE}$ of the $(FCS)_{50}Pt_{50}$ composite films is ~7 times larger [see Fig. 6(b)] than the as-deposited FCS alloy film owing to its significantly smaller $\rho_{xx}$ [see Fig. 6(c)] due to Pt doping, which has much lower resistivity.

To further understand the origin of the enhancement in $S_{ANE}$ in the $(FCS)_{50}Pt_{50}$ composite film, the contributions of $S_I$ and $S_{II}$ to $S_{ANE}$ have been evaluated using the experimentally obtained values as shown in Fig. 6(a) and 6(c-d). The data reveal that the enhancement in $S_{ANE}$ in the $(FCS)_{50}Pt_{50}$ composite is due to the enhancement in the $S_I$ term, and there is no significant variation in the $S_{II}$ term. To further clarify the origin of the large $S_I$ term in the $(FCS)_{50}Pt_{50}$ film, $\alpha_{xy}$ was evaluated for the $(FCS)_{50}Pt_{50}$ composite film using the relation $\alpha_{xy} = S_I/\rho_{xx}$ [see Fig. 6(d)]. The $\alpha_{xy}$ value was found to be more than two times larger than that of the FCS alloy, clarifying its dominant contribution in the enhancement of $S_{ANE}$ for the $(FCS)_{50}Pt_{50}$ composite alloy film. While the microscopic origin of such behavior requires a more detailed investigation in a future study, it can be speculated to have a similar physical mechanism as discussed in previous studies of FM/HM films[31–33], assuming that these composite alloys have the maximum number of interfaces between FCS and Pt.

To distinguish interfacial effects in the FCS-Pt composite films, we investigated its modulation in FCS/Pt multilayers. For this study, [FCS ($t_{FCS}$)/Pt (0.5 nm)]$_n$ multilayer films were prepared by repeating the FCS and Pt layers with the repetition number $n$. The Pt layer thickness was fixed at 0.5 nm across all stacks, whereas different stacks were fabricated, each with an FCS layer thickness ($t_{FCS}$) fixed at 0.5, 1.0, 2.0, 5.0, and 10.0 nm. The $n$ value for each film was determined so that the total thickness of FCS layers in the multilayer was fixed at 50 nm (*i.e.*, $n = 50/t_{FCS}$). All the other fabrication conditions remained the same as discussed in Section II.A. The uniform $(FCS)_{50}Pt_{50}$ composite film was compared with the ultra-thin [FCS (0.5 nm)/Pt (0.5 nm)]$_{100}$ multilayer stacks, considering the possibility of natural mixing in ultra-thin layers.[30] To prevent oxidation, the $(FCS)_{50}Pt_{50}$ film was capped with a 2-nm-thick Al layer. Since the maximum $S_{ANE}$ was obtained in the as-deposited FCS film, only the as-deposited

films were studied. The structural and transverse thermoelectric properties of the as-deposited multilayer films and $(FCS)_{50}Pt_{50}$ film of uniform compositions were then evaluated and compared to understand the origin of the enchantment of $S_{ANE}$ in $(FCS)_{50}Pt_{50}$.

The detailed analysis of the experimental data of the [FCS ($t_{FCS}$)/Pt (0.5 nm)]$_n$ multilayer films is summarized in the supplementary material (see Note S1). The similarity in XRD patterns (see Figure S1) between the FCS (0.5 nm)/Pt (0.5 nm) multilayer and the uniform $(FCS)_{50}Pt_{50}$ film suggests the possibility of natural intermixing at the interfaces of such ultrathin layers.[30] This intermixing can result in a compositionally mixed region, making the multilayer structure exhibit an XRD pattern similar to that of the uniform film.

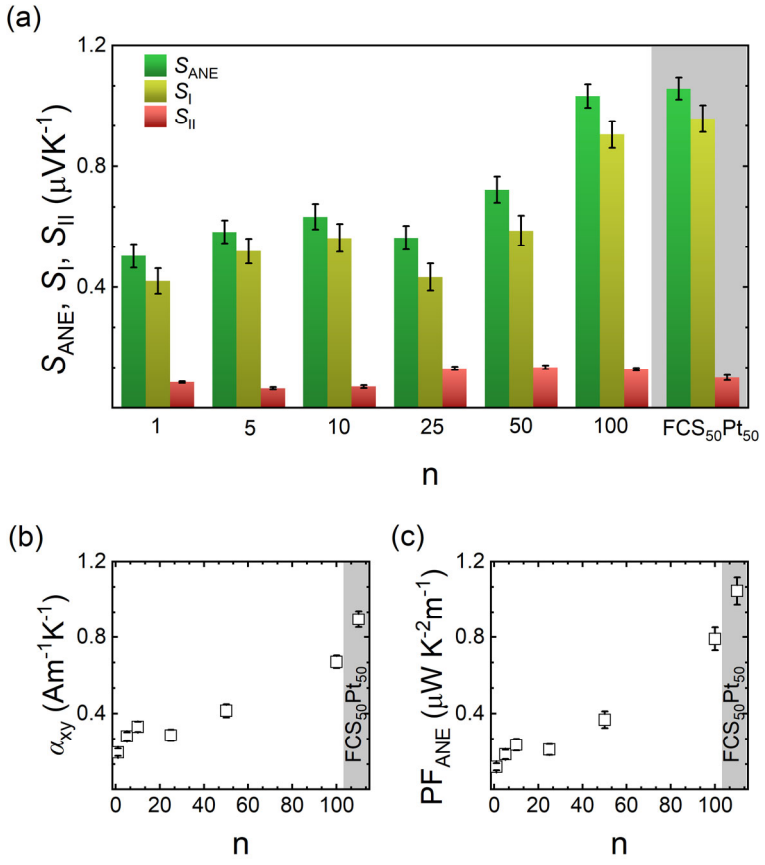


Fig. 7. (a) Extracted values of $S_{ANE}$, $S_I$ and $S_{II}$ as a function of $n$, (b) $\alpha_{xy}$ versus $n$, and (c) $PF_{ANE}$ versus $n$ plot. In all the graphs, the shaded data point represents the $(FCS)_{50}Pt_{50}$ uniform composite film for comparison with the multilayer films.

Figure 7(a) summarizes the values of $S_{ANE}$, $S_I$, and $S_{II}$ for the [FCS ($t_{FCS}$)/Pt (0.5 nm)]$_n$ multilayers alongside the $(FCS)_{50}Pt_{50}$ film. It is clearly observed that there is a sharp increase in $S_{ANE}$ for the $n$ = 100 multilayer film, which is nearly the same for the uniform $(FCS)_{50}Pt_{50}$

composite film. The result also shows that the major contribution to $S_{ANE}$ comes from the $S_I$ term, although $S_{II}$ increases with increasing $n$. To gain deeper insight into the origin of the large $S_I$ term, we further evaluated $\alpha_{xy}$ using the relation $\alpha_{xy} = S_I/\rho_{xx}$, and observed a steady increase with $n$, reaching its highest value the $(FCS)_{50}Pt_{50}$ film [see Fig. 7(b)]. This detailed analysis of $S_{ANE}$ components clearly demonstrates that the significant enhancement in $\alpha_{xy}$ is primarily responsible for the large $S_I$ term in the multilayer films as well as in the $(FCS)_{50}Pt_{50}$ composite film. To assess the ANE performance of the multilayers, we also evaluate the $PF_{ANE}$. Similar to $\alpha_{xy}$, a huge increment (575 %) in $PF_{ANE}$ can be obtained due to the concerted action of the increase in $S_{ANE}$ and significant decrease in $\rho_{xx}$ with increase in $n$ from [Fig. 7(c)]. Notably, the $PF_{ANE}$ value for the $(FCS)_{50}Pt_{50}$ film surpasses that of the $n$ = 100 multilayer, which is expected given its higher $\alpha_{xy}$ and lower $\rho_{xx}$. These experimental findings highlight that multilayering with Pt and increasing interface density serve as effective strategies for enhancing ANE performance in disordered FCS alloy films.

The observed enhancement may originate from several mechanisms, including interfacial spin orbit coupling, proximity induced magnetism in Pt, and possible intermixing or alloying at the FCS/Pt interfaces.[10,31-33] As the number of bilayer repetitions $n$ increases, corresponding to a reduction in the FCS layer thickness and an increase in interface density, $S_{ANE}$ initially increases monotonically up to $n < 25$. This behavior is consistent with an enhanced interfacial contribution to the ANE. However, for $n$ = 25, a noticeable reduction in $S_{ANE}$ is observed, followed by a rapid increase for $n$ = 100.[10,31] At very high $n$ values, the ultra-thin FCS layers may interdiffuse, forming an alloy of FCS and Pt. This intermixing may lead to the formation of an effective FCS-Pt composite phase with enhanced spin orbit interaction distributed throughout the film volume rather than being confined to discrete interfaces. Consequently, the superior ANE performance observed in the FCS-Pt composite can be attributed to enhanced spin orbit interaction and interfacial effects arising from intermixing between FCS and Pt. This result demonstrates that FM-NM composite film using a heavy metal as NM, such as Pt can provide an effective pathway for enhancing the transverse thermoelectric performance of a magnetic material, including Heusler alloys. These outcomes provide guidelines to develop new composite ANE materials with enhanced transverse thermoelectric performance, which can potentially be realized in bulk or ribbon-type composite systems as well.

## IV. CONCLUSION

In summary, we have systematically investigated the effect of post-deposition annealing temperatures and the consequent evolution of crystalline ordering on the transverse magneto-thermoelectric conversion properties of FCS Heusler alloys. Our study finds that $S_{ANE}$ in the FCS films is relatively lower compared to traditional Heusler alloys, primarily due to the significantly smaller $\alpha_{xy}$. However, the study revealed that in contrast to conventional Heusler alloys behavior, the as-deposited amorphous/disordered FCS film exhibits a larger $S_{ANE}$ than its crystalline counterparts, attributed to higher electrical resistivity $\rho_{xx}$, while $\alpha_{xy}$ remains comparable. Furthermore, by forming composite alloys with heavy metal element Pt, both the $\alpha_{xy}$ and $S_{ANE}$ could be nearly doubled in the FCS films. Notably, the power factor is enhanced by nearly six times in the composite films. These findings demonstrate that, beyond traditional FM/HM multilayer structures, FM-HM composites can also serve as an effective strategy for enhancing the magneto-thermoelectric conversion performance of ferromagnetic materials, including Heusler alloys. Thus, this study provides new guidelines for the design and development of advanced ANE materials.

## SUPPLEMENTARY MATERIAL

The supplementary material includes details on the transverse thermoelectric properties of FCS/Pt multilayer films as a function of interface number ($n$) and the annealing temperature dependence of magnetization in uniform FCS films. Figure S1 shows the multilayer schematics and XRD patterns. Figure S2 presents the magnetic field dependence of $V/d$ and $\nabla T$ dependence of $E_{ANE}$. Figure S3 compares the thermoelectric performance of multilayer films with the uniform $(FCS)_{50}Pt_{50}$ composite film. Figure S4 shows the isothermal magnetization curves of as-deposited and annealed FCS films and their saturation magnetization compared with bulk FCS.

## ACKNOWLEDGEMENTS

The authors thank R. Nagasawa and V. Kushwaha for technical support and R. Iguchi and Y. Sakuraba for valuable discussions. This work was partially supported by ERATO “Magnetic Thermal Management Materials Project" (No. JPMJER2201) from JST, Japan; Grant-in-Aid for Scientific Research (S) (No. 22H04965) from JSPS KAKENHI, Japan; and NEC Corporation. SB was supported by the International Cooperative Graduate Program between

the National Institute for Materials Science and the Indian Institute of Technology Guwahati. RM was partially supported by JSPS through the "JSPS Postdoctoral Fellowship for Research in Japan (Standard)" (P21064).

## AUTHOR DECLARATIONS

### Conflict of Interest

The authors have no conflicts to disclose.

### Data availability statement

The data that support the findings of this study are available from the corresponding author upon reasonable request.

### References

[1] J. Wang, Y. Lau, W. Zhou, T. Seki, Y. Sakuraba, T. Kubota, K. Ito, and K. Takanashi, "Strain-induced large anomalous Nernst effect in polycrystalline $Co_2MnGa$/AlN multilayers," Adv. Electron. Mater. **8**, 2101380 (2022).

[2] K. Uchida, and J.P. Heremans, "Thermoelectrics: From longitudinal to transverse," Joule **6**, 2240–2245 (2022).

[3] K. Uchida, S. Takahashi, K. Harii, J. Ieda, W. Koshibae, K. Ando, S. Maekawa, and E. Saitoh, "Observation of the spin Seebeck effect," Nature **455**, 778–781 (2008).

[4] T. Seki, R. Iguchi, K. Takanashi, and K. Uchida, "Relationship between anomalous Ettingshausen effect and anomalous Nernst effect in an FePt thin film," J. Phys. D. Appl. Phys. **51**, 254001 (2018).

[5] S. N. Guin, K. Manna, J. Noky, S.J. Watzman, C. Fu, N. Kumar, W. Schnelle, C. Shekhar, Y. Sun, J. Gooth, and C. Felser, "Anomalous Nernst effect beyond the magnetization scaling relation in the ferromagnetic Heusler compound $Co_2MnGa$," NPG Asia Mater. **11**, 16 (2019).

[6] Y. Sakuraba, K. Hyodo, A. Sakuma, and S. Mitani, "Giant anomalous Nernst effect in the $Co_2MnAl_{1-x}Si_x$ Heusler alloy induced by Fermi level tuning and atomic ordering," Phys. Rev. B **101**, 134407 (2020).

[7] Y. Sakuraba, "Potential of thermoelectric power generation using anomalous Nernst effect in magnetic materials," Scr. Mater. **111**, 29–32 (2016).

[8] T. Yamazaki, T. Seki, R. Modak, K. Nakagawara, T. Hirai, K. Ito, K. Uchida, and K. Takanashi, "Thickness dependence of anomalous Hall and Nernst effects in Ni-Fe thin films," Phys. Rev. B **105**, 214416 (2022).

[9] K. Uchida, W. Zhou, and Y. Sakuraba, "Transverse thermoelectric generation using magnetic materials," Appl. Phys. Lett. **118**, 140504 (2021).

[10] T. Seki, Y. Sakuraba, K. Masuda, A. Miura, M. Tsujikawa, K. Uchida, T. Kubota, Y. Miura, M. Shirai, and K. Takanashi, "Enhancement of the anomalous Nernst effect in Ni/Pt superlattices," Phys. Rev. B **103**, L020402 (2021).

[11] H. Adachi1, F. Ando, T. Hirai, R. Modak, M.A. Grayson, and K. Uchida, "Fundamentals and advances in transverse thermoelectrics," Appl. Phys. Express **18**, 090101 (2025).

[12] W. Zhou, and Y. Sakuraba, "Heat flux sensing by anomalous Nernst effect in Fe-Al thin films on a flexible substrate," Appl. Phys. Express **13**, 043001 (2020).

[13] F. Ando, T. Hirai, and K. Uchida, "Permanent-magnet-based transverse thermoelectric generator with high fill factor driven by anomalous Nernst effect," APL Energy **2**, 016103 (2024).

[14] T. Hirai, F. Ando, H. Sepehri-Amin, and K. Uchida, "Hybridizing anomalous Nernst effect in artificially tilted multilayer based on magnetic topological material," Nat. Commun. **15**, 9643 (2024).

[15] H. Tanaka, T. Higo, R. Uesugi, K. Yamagata, Y. Nakanishi, H. Machinaga, and S. Nakatsuji, "Roll-to-roll printing of anomalous Nernst thermopile for direct sensing of perpendicular heat flux," Adv. Mater. **35**, 2303416 (2023).

[16] S.J. Watzman, R.A. Duine, Y. Tserkovnyak, S.R. Boona, H. Jin, A. Prakash, Y. Zheng, and J.P. Heremans, "Magnon-drag thermopower and Nernst coefficient in Fe, Co, and Ni," Phys. Rev. B **94**, 144407 (2016).

[17] L.E. Bell, "Cooling, heating, generating power, and recovering waste heat with thermoelectric systems," Science. **321**, 1457–1461 (2008).

[18] C.D.W. Cox, A.J. Caruana, M.D. Cropper, and K. Morrison, "Anomalous Nernst effect in $Co_2MnSi$ thin films," J. Phys. D: Appl. Phys. **53**, 035005 (2020).

[19] H. Reichlova, R. Schlitz, S. Beckert, P. Swekis, A. Markou, Y.C. Chen, D. Kriegner, S. Fabretti, G. Hyeon Park, A. Niemann, S. Sudheendra, A. Thomas, K. Nielsch, C. Felser, and

S.T.B. Goennenwein, "Large anomalous Nernst effect in thin films of the Weyl semimetal $Co_2MnGa$," Appl. Phys. Lett. **113**, 212405 (2018).

[20] R. Modak, K. Goto, S. Ueda, Y. Miura, K. Uchida, and Y. Sakuraba, "Combinatorial tuning of electronic structure and thermoelectric properties in $Co_2MnAl_{1-x}Si_x$ Weyl semimetals," APL Mater. **9**, 031105 (2021).

[21] G.K. Shukla, A.K. Jena, N. Shahi, K.K. Dubey, I. Rajput, S. Baral, K. Yadav, K. Mukherjee, A. Lakhani, K. Carva, S.-C. Lee, S. Bhattacharjee, and S. Singh, "Atomic disorder and Berry phase driven anomalous Hall effect in a $Co_2FeAl$ Heusler compound," Phys. Rev. B **105**, 035124 (2022).

[22] T. Yamauchi, Y. Hamada, Y. Kurokawa, and H. Yuasa, "Anomalous Nernst effect dependence on composition in $Fe_{100-x}$ $Rh_x$ alloys," Jpn. J. Appl. Phys. **61**, SC1019 (2022).

[23] Q. Wang, Z. Wen, T. Kubota, T. Seki, and K. Takanashi, "Structural-order dependence of anomalous Hall effect in $Co_2MnGa$ topological semimetal thin films," Appl. Phys. Lett. **115**, 252401 (2019).

[24] F. Mende, J. Noky, S.N. Guin, G.H. Fecher, K. Manna, P. Adler, W. Schnelle, Y. Sun, C. Fu, and C. Felser, "Large anomalous Hall and Nernst effects in high Curie-temperature iron-based Heusler compounds," Adv. Sci. **8**, 2100782 (2021).

[25] A.T. Breidenbach, H. Yu, T.A. Peterson, A.P. McFadden, W.K. Peria, C.J. Palmstrøm, and P.A. Crowell, "Anomalous Nernst and Seebeck coefficients in epitaxial thin film $Co_2MnAl_xSi_{1-x}$ and $Co_2FeAl$," Phys. Rev. B **105**, 144405 (2022).

[26] Y. Nishino, H. Sumi, and U. Mizutani, "Transport and magnetic properties of the Heusler-type $Fe_{2-x}V_{1+x}Al$ system ($-0.01 \leq x \leq 0.08$)," Phys. Rev. B **71**, 094425 (2005).

[27] R. Uesugi, T. Higo, and S. Nakatsuji, "Giant anomalous Nernst effect in polycrystalline thin films of the Weyl ferromagnet $Co_2MnGa$," Appl. Phys. Lett. **123**, 252401 (2023).

[28] J. Noky, Q. Xu, C. Felser, and Y. Sun, "Large anomalous Hall and Nernst effects from nodal line symmetry breaking in $Fe_2MnX$ (X = P, As, Sb)," Phys. Rev. B **99**, 165117 (2019).

[29] J. Noky, "Giant anomalous Hall and Nernst effect in magnetic cubic Heusler compounds," Npj Comput. Mater. **6**, 77 (2020).

[30] R. Modak, Y. Sakuraba, T. Hirai, T. Yagi, H. Sepehri-Amin, W. Zhou, H. Masuda, T. Seki, K. Takanashi, T. Ohkubo, and K. Uchida, "Sm-Co-based amorphous alloy films for zero-field

operation of transverse thermoelectric generation," Sci. Technol. Adv. Mater. **23**, 767–782 (2022).

[31] K. Uchida, T. Kikkawa, T. Seki, T. Oyake, J. Shiomi, Z. Qiu, K. Takanashi, and E. Saitoh, "Enhancement of anomalous Nernst effects in metallic multilayers free from proximity-induced magnetism," Phys. Rev. B **92**, 094414 (2015).

[32] R. Ramos, T. Kikkawa, A. Anadón, I. Lucas, T. Niizeki, K. Uchida, P.A. Algarabel, L. Morellón, M.H. Aguirre, M.R. Ibarra, and E. Saitoh, "Interface-induced anomalous Nernst effect in $Fe_3O_4$/Pt-based heterostructures," Appl. Phys. Lett. **114**, 113902 (2019).

[33] C. Fang, C.H. Wan, Z.H. Yuan, L. Huang, X. Zhang, H. Wu, Q.T. Zhang, and X.F. Han, "Scaling relation between anomalous Nernst and Hall effect in $[Pt/Co]_n$ multilayers," Phys. Rev. B **93**, 054420 (2016).

[34] S. Daimon, R. Iguchi, T. Hioki, E. Saitoh, and K. Uchida, "Thermal imaging of spin Peltier effect," Nat. Commun. **7**, 13754 (2016).

[35] K. Uchida, S. Daimon, R. Iguchi, and E. Saitoh, "Observation of anisotropic magneto-Peltier effect in nickel," Nature **558**, 95–99 (2018).

[36] A. Miura, H. Sepehri-Amin, K. Masuda, H. Tsuchiura, Y. Miura, R. Iguchi, Y. Sakuraba, J. Shiomi, K. Hono, and K. Uchida, "Observation of anomalous Ettingshausen effect and large transverse thermoelectric conductivity in permanent magnets," Appl. Phys. Lett. **115**, 222403 (2019).

[37] A. Miura, K. Masuda, T. Hirai, R. Iguchi, T. Seki, Y. Miura, H. Tsuchiura, K. Takanashi, and K. Uchida, "High-temperature dependence of anomalous Ettingshausen effect in $SmCo_5$-type permanent magnets," Appl. Phys. Lett. **117**, 082408 (2020).

[38] K. Uchida, M. Sasaki, Y. Sakuraba, R. Iguchi, S. Daimon, E. Saitoh & M. Goto, Combinatorial investigation of spin-orbit materials using spin Peltier effect, Sci Rep **8**, 16067 (2018).

[39] H. Masuda, R. Modak, T. Seki, K. Uchida, Y.-C. Lau, Y. Sakuraba, R. Iguchi, and K. Takanashi, "Large spin-Hall effect in non-equilibrium binary copper alloys beyond the solubility limit," Commun. Mater. **1**, 75 (2020).

[40] H. Nakayama, K. Masuda, J. Wang, A. Miura, K. Uchida, M. Murata, and Y. Sakuraba, "Mechanism of strong enhancement of anomalous Nernst effect in Fe by Ga substitution," Phys. Rev. Mater. **3**, 114412 (2019).

[41] K. Sumida, Y. Sakuraba, K. Masuda, T. Kono, M. Kakoki, K. Goto, W. Zhou, K. Miyamoto, Y. Miura, T. Okuda, and A. Kimura, "Spin-polarized Weyl cones and giant anomalous Nernst effect in ferromagnetic Heusler films," Commun. Mater. **1**, 89 (2020).

[42] S. Kurdi, Y. Sakuraba, K. Masuda, H. Tajiri, B. Nair, G.F. Nataf, M.E. Vickers, G. Reiss, M. Meinert, S.S. Dhesi, M. Ghidini, and Z.H. Barber, "Quantitative atomic order characterization of a $Mn_2FeAl$ Heusler epitaxial thin film," J. Phys. D. Appl. Phys. **55**, 185305 (2022).

[43] H. Luo, Z. Zhu, L. Ma, S. Xu, H. Liu, J. Qu, Y. Li, and G. Wu, "Electronic structure and magnetic properties of $Fe_2YSi$ (Y = Cr, Mn, Fe, Co, Ni) Heusler alloys: a theoretical and experimental study," J. Phys. D. Appl. Phys. **40**, 7121–7127 (2007).

[44] C. Sterwerf, S. Paul, B. Khodadadi, M. Meinert, J.M. Schmalhorst, M. Buchmeier, C.K.A. Mewes, T. Mewes, and G. Reiss, "Low Gilbert damping in $Co_2FeSi$ and $Fe_2CoSi$ films," J. Appl. Phys. **120**, 083904 (2016).

[45] N. Shahi, A.K. Jena, G.K. Shukla, V. Kumar, S. Rastogi, K.K. Dubey, I. Rajput, S. Baral, A. Lakhani, S.C. Lee, S. Bhattacharjee, and S. Singh, "Antisite disorder and Berry curvature driven anomalous Hall effect in the spin gapless semiconducting $Mn_2CoAl$ Heusler compound," Phys. Rev. B **106**, 245137 (2022).

[46] T. Saito, and D. Nishio-Hamane, "Magnetic and thermoelectric properties of melt-spun ribbons of $Fe_2XAl$ (X = Co, Ni) Heusler compounds," J. Appl. Phys. **124**, 075105 (2018).

[47] K. Tanikawa, S. Oki, S. Yamada, K. Mibu, M. Miyao, and K. Hamaya, "Effect of Co-Fe substitution on room-temperature spin polarization in $Co_{3-x}Fe_xSi$ Heusler-compound films," Phys. Rev. B - Condens. Matter Mater. Phys. **88**, 014402 (2013).

[48] M. Li, H. Pi, Y. Zhao, T. Lin, Q. Zhang, X. Hu, C. Xiong, Z. Qiu, L. Wang, Y. Zhang, J. Cai, W. Liu, J. Sun, F. Hu, L. Gu, H. Weng, Q. Wu, S. Wang, Y. Chen, and B. Shen "Large anomalous Nernst effects at room temperature in $Fe_3Pt$ thin films," Adv. Mater. **35**, 2301339 (2023).